Multifunctionality of Layered Materials

Septiany, Liany

DOI:
10.33612/diss.182500502

Chapter 6

Tuning The Magnetic Exchange Energy of $(CH_3NH_3)_2MnCl_4$ Through Localized Anion Vacancies

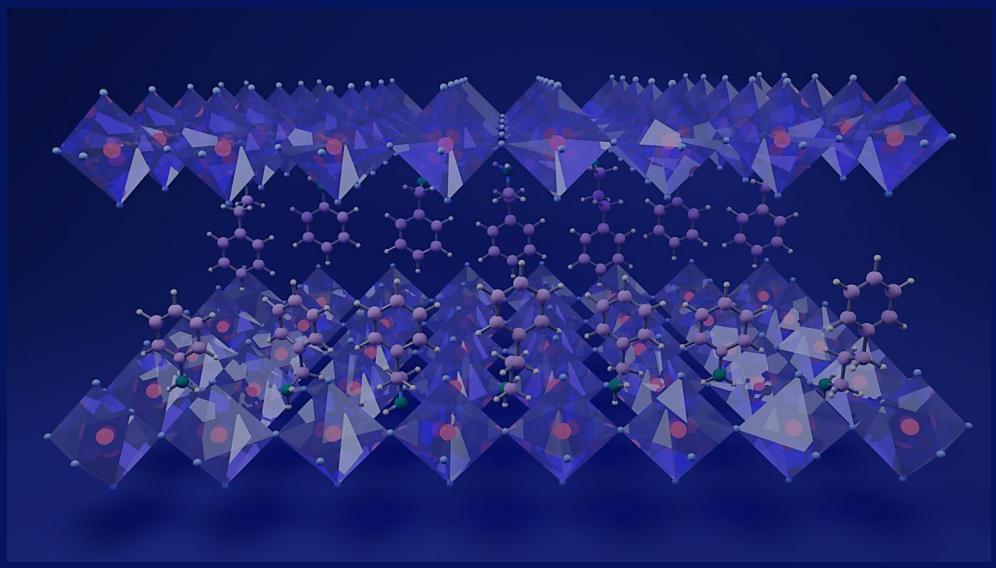

L. Septiany, T. Idema, M. Aidi, J. Baas, G.R. Blake

Tuning The Magnetic Exchange Energy of $(CH_3NH_3)_2MnCl_4$ Through Localized Anion Vacancies

Abstract

$(CH_3NH_3)_2MnCl_4$ has been used as an ideal system in which to study two-dimensional Heisenberg antiferromagnetism. In this chapter, we study the effect of varying the halide concentration in single crystals of $(CH_3NH_3)_2MnCl_{4-x}$ on their crystal structure and magnetic properties. We observe crystal twinning, which can lead to difficulties in structural characterization, especially when assigning the correct space group. We investigate the possibility of a spin-crossover in this material; previous studies have reported effective paramagnetic moments consistent with both high spin and low spin states in layered manganese chloride-based perovskites with short alkyl chain cations. We find that all samples show two-dimensional antiferromagnetism with a transition to three-dimensional canted antiferromagnetic ordering at ~45K. We also find that with increasing the halide deficiency, the magnetic exchange energy decreases, most likely due to local anion vacancies.

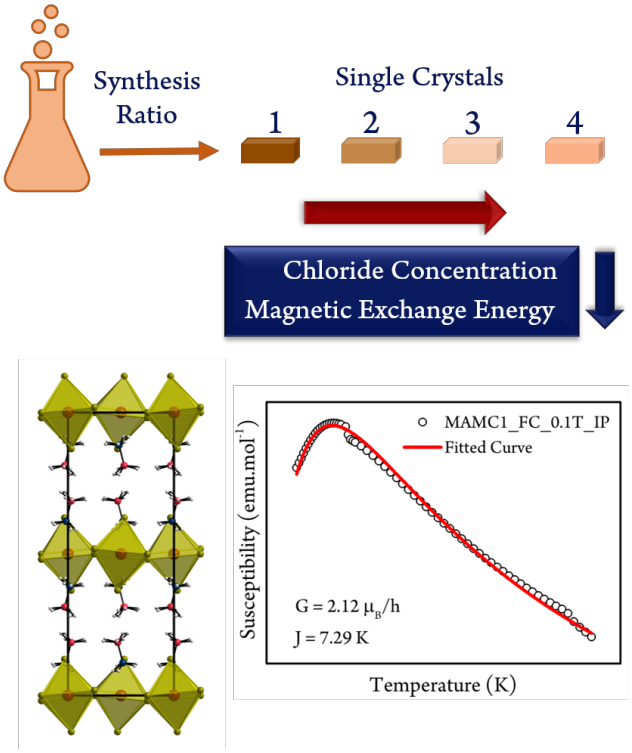

6.1 Introduction

The magnetic properties of $(CH_3NH_3)_2MnCl_4$ (referred to hereafter as MAMC) have been studied since the 1970s[1–12]. The structure of MAMC consists of stacked $MnCl_6$ sheets separated by a bilayer of (CH_3NH_3) molecules and is analogous to the K_2NiF_4-type structure. MAMC is known to exhibit four different structures across the temperature range of 90-400K: a low-temperature monoclinic (LTM) phase, low-temperature tetragonal (LTT) phase, room-temperature orthorhombic (RTO) phase, and high-temperature tetragonal (HTT) phase. The driving force of these structural phase transitions is believed to arise from both different degrees of orientational order of the methylammonium (MA) molecules and cooperative tilting of the $MnCl_6$ octahedra. Beside its interesting structural properties, MAMC is known to exhibit two-dimensional magnetic properties. Van Amstel and de Jongh reported the onset of antiferromagnetic ordering with a transition temperature (T_N) at 47±3K, below which anisotropy is exhibited,[1] manifested by a magnetization response that depends on the crystal direction along which the measurement is performed. Curély et al. later carried out theoretical studies of 2D Heisenberg antiferromagnetic systems with a square magnetic lattice (including MAMC), and proposed models to explain the magnetic behaviour in such systems.[13–16] Although MAMC is considered to be a 2D antiferromagnet, magnetic exchange in the out-of-plane direction is not negligible. It has been shown that for short organic cations (of 1 to 4 carbon atoms in length), the exchange energy decreases as the interlayer distance increases.[17] For longer organic cations (>8 carbon atoms), the Dzyaloshinski-Moriya (or antisymmetric) exchange interaction and Ising anisotropy both play a more prominent role. The Dzyaloshinki-Moriya interaction is responsible for spin canting which gives rise to a weak in-plane ferromagnetic moment. The Ising anisotropy arises due to competing magnetic interactions and along with the Dzyaloshinki-Moriya interaction can alter the 2D characteristics. Therefore, the interlayer distance is not the only factor that affects the magnetic properties of layered perovskites.

MAMC is reported to adopt a high-spin state (S = 5/2) with superexchange interactions between Mn^{2+} cations via the Cl^- anions.[1] However, $(C_2H_5NH_3)_2MnCl_4$ with a similar crystal structure has been reported to show a low-spin state (S = ½).[18] These observations hint at the

possibility of spin-crossover (SCO) behaviour in this family of compounds. The spin crossover (SCO)[19,20] is a phenomenon where the magnetic metal ion undergoes a transition between a high spin (HS) and a low spin (LS) state due to external stimuli, such as pressure, temperature, or light irradiation.[19,20] SCO transitions can be found in many metal-organic complexes in which the transition metal ions are coordinated and/or linked by flexible organic ligands. The transition metals in such complexes are usually first-row elements with an electronic configuration of d^4-d^7. However, thus far very few hybrid perovskites have been reported to show SCO phenomena.[21] Different to most metal-organic complexes, which usually exhibit single molecule magnet (SMM) behaviour, hybrid perovskites have a long-range extended network which is advantageous for cooperative magnetic order. According to crystal field theory, the possibility for a SCO is determined by the magnitude of the crystal field splitting energy ($\Delta = 10Dq$). The magnitude of Δ typically depends on both the nature of the ligand and on the length of the metal-ligand bonds. To obtain an appropriate SCO compound, a suitable combination of the transition metal and organic linker should be identified such that the t_{2g} and e_g energy levels (in the case of octahedral coordination) are close enough for a SCO to be driven by a small change of energy due to temperature or light. Several studies have investigated the effect of structural features on the electronic configuration of the d-orbitals which in turn affects the SCO.[22–25] A theoretical study of the hybrid perovskite dimethylammonium manganese formate showed that the metal-anion bond length has a critical value which determines whether the compound exhibits a low-spin or high-spin state.[24]

The current study investigates the effect of halide concentration/vacancies on the structural and magnetic properties of MAMC. While the structural properties show only subtle changes in bond distances and angles with increasing halide deficiency, consistent with contraction of the structure, the magnetic properties show a more pronounced effect. We find that with decreasing halide concentration, the exchange energy decreases by up to 1.3 K due to anion vacancies. We also investigate the possibility of whether anion vacancies can induce a change in the metal coordination, affecting the crystal field splitting energy.

6.2 Experimental Details

6.2.1 Crystal Growth

Table 6.1 Concentrations of precursors in synthesis

Compound	[HCl]	[MA]	[$MnCl_2$]	Crystal Colour
MAMC1	8mmol	8mmol	4mmol	Brown
MAMC2	6mmol	8mmol	4mmol	Light brown
MAMC3	4mmol	8mmol	4mmol	Light orange
MAMC4	4mmol	4mmol	4mmol	Pink-orange

MAMC was synthesized by mixing anhydrous $MnCl_2$ (beads, Sigma Aldrich; ≥ 99%), CH_3NH_3 (Sigma Aldrich; 33 wt.% in absolute ethanol), and HCl (Sigma Aldrich; 1.25 M in absolute ethanol) with absolute ethanol as solvent. The molar ratios of the precursors in different preparations are given in Table 6.1. Single crystals were grown by the slow evaporation method at 60°C. After ~1week, single crystals were obtained from the solution as platelets with different colors depending on the HCl concentration (see Fig. 6.3).

6.2.2 X-Ray Diffraction

A Bruker D8 Venture diffractometer operating with Mo-K*α* radiation was used for single crystal X-ray diffraction (XRD) measurement. The diffractometer was equipped with a Photon 100 area detector and a Triumph monochromator. The crystal was placed on a glass fibre using a commercial acrylate glue for room and high-temperature measurement. For low-temperature measurement the crystals were mounted in a fibre loop using cryo-oil and cooled in a nitrogen flow using an Oxford Cryostream Plus. The Bruker APEX III software was used to process the data. Structure solution and refinement was carried out using direct methods and the SHELX97 software[26].

For powder XRD measurement at room temperature, the crystals were hand-ground into a fine powder using an agate mortar and pestle. A Bruker D8 Advance diffractometer operating with a Cu-K*α* source was used for the measurements. The structural parameters were refined by the Rietveld refinement using the GSAS software [27].

6.2.3 Magnetic Measurement

A Quantum Design MPMS SQUID magnetometer was used for the magnetic measurements. Single crystals that were large enough were measured along two different crystal orientations, whereas samples for which large enough crystals were not available were measured by stacking several small plate-like crystals together. The temperature dependence of the DC magnetization was measured on warming from 5-300K after field cooling in 1000Oe. Field-dependent magnetization measurements were carried out up to 6T at 10K after cooling in zero magnetic field.

6.3 Results and Discussion

6.3.1 Structural Analysis

The structure of MAMC has been widely reported. It undergoes three structural phase transitions, two of which are shown in Fig. 6.1. The LTT structure has the tetragonal $P4_2/ncm$ space group, as shown in Fig. 6.1a. Here the $MnCl_6$ octahedra are buckled and can be described by the Glazer notation $(a^+b^0c^0)(a^0b^-c^0)$.[28] The RTO structure is orthorhombic with space group Cmca. Compared to the LTT structure, the RTO phase is more symmetric, in which the buckling of the $MnCl_6$ octahedra is less apparent and the organic cations are almost parallel to the c-axis. The RTO phase transforms to the HTT phase at 398K, which can be described with a smaller in-plane cell parameter such that the RTO cell parameter is a $\sqrt{2}$ multiple of that of the HTT phase. This phase transition arises due to an order to disorder transition of the MA cation.

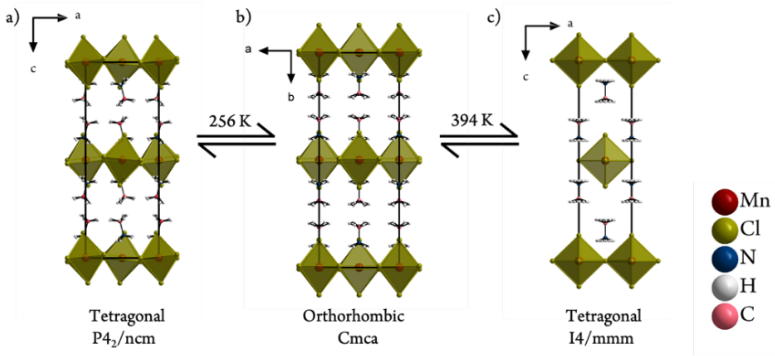

Figure 6.1 *Crystal structure of MAMC at a) 100K, b) 300K, and c) 400K.*

Table 6.2 Structural parameters of MAMC1 at different temperatures.

Parameter	100K	300K	400K
Crystal System	Tetragonal	Orthorhombic	Tetragonal
Space group	$P4_2/ncm$	Cmca	I4/mmm
a (Å)	7.2185(5)	7.2578 (11)	5.1450(6)
b (Å)	7.2185(5)	19.4299(29)	5.1450(6)
c (Å)	19.2972(22)	7.2547(11)	19.5297(37)
V (Å^3)	1005.51	1023.05	516.97
Z	4	4	1
density (g/cm^3)	1.723	1.694	1.676
goodness of fit	0.953	1.060	1.127
R indices	0.0336	0.0616	0.0306
largest diff peak/hole	0.42/-0.63	0.26/-0.35	0.26/-0.62

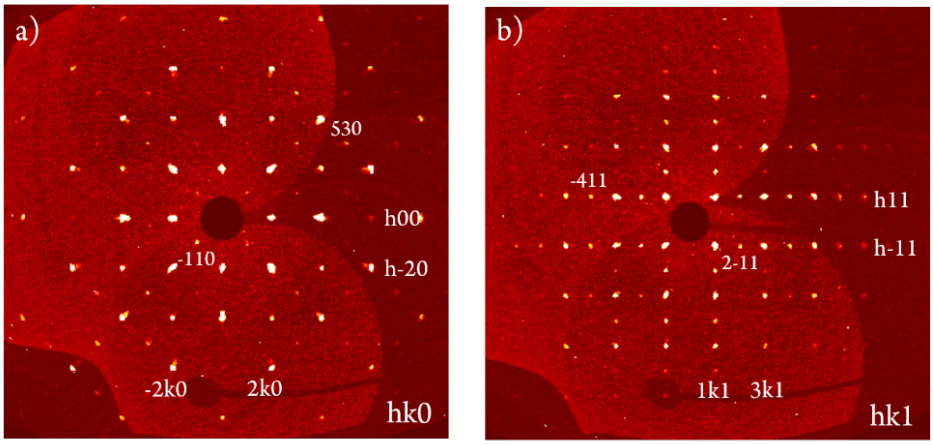

Figure 6.2 *Precession images obtained from SC-XRD data for a) (hk0) and b) (hk1) reciprocal lattice planes.*

In our diffraction measurements of single crystals we found evidence for crystal twinning, which has not been reported in the literature for MAMC and can lead to confusion in the structure determination process. The unit cell parameters of the three phases of MAMC Sample 1 are listed in Table 6.2. On initial inspection the precession images (reciprocal lattice planes) constructed from raw single-crystal XRD data collected at room temperature do not obey all the reflection conditions related to the Cmca space group of the RTO structure. A C-centred structure should obey the reflection condition (hkl, h+k=2n), but from the (hk1) plane in Fig. 6.2b this is not the case. However, this condition may still hold if a second twin domain is present where the a and c-axes are swapped. Here the second twin domain is formed by 90 degrees rotation around the b-axis (described by the twin matrix [0 0 1 0 1 0 -1 0 0]) of the first twin domain. This type of twinning is common in orthorhombic structures where two axes are of similar length. The two-domain scenario is supported by the observation in Fig. 6.2b that spots with (h+k = odd) are weaker, since only the second domain would contribute, whereas the (h+k = even) spots have intensity contributions from both domains. The twinning also leads to the apparent violation of the Cmca reflection condition (hk0, h, k = 2n) (Fig. 6.2a) because 0kl spots are superimposed on this plane, where l can be even or odd.

Attempts were first made to solve the structure using the orthorhombic primitive space group Pcc2, the only space group with systematic absences that agree with those observed in Fig. 6.2 when the possibility of twinning is neglected. The inorganic part of the structure could be solved approximately using direct methods and assuming a single domain. However, the full structure could only be solved with difficulty, especially when unambiguously assigning positions to the carbon and nitrogen atoms of the MA molecule. Since the data quality appears good (the spots are sharp and well defined as apparent in Fig. 6.2), this difficulty in solving and refining the full structure can be considered a warning sign of crystal twinning. In contrast, structure solution and refinement in the orthorhombic C-centered Cmca space group, with the twin law described above, proceeded much more smoothly and the fit to the data was significantly better than that assuming the primitive Pcc2 cell.

Structure solutions of the LTT and HTT phases were unambiguous and agree with previous reports since this type of twinning is not found in tetragonal structures. The refined unit cell

parameters of the other MAMC samples are listed in Appendix A, Table 6.5-6.7. The in-plane lattice parameter of the LTT phase at 100 K decreases slightly with decreasing halide concentration, giving a corresponding decrease in unit cell volume. The effect of halide concentration can be seen more clearly from the crystal colour and the powder XRD data. The crystal colour gradually becomes lighter with decreasing HCl concentration, as mentioned in Table 6.1 and shown in Fig. 6.3, showing the possibility of a variation in the bandgap. The powder XRD data obtained from ground crystals shows the presence of a secondary phase when the halide concentration deviates from the stoichiometric ratio. As presented in Fig. 6.4, for the MAMC2 sample prepared using a Mn:Cl ratio of 1 : 3.5, peaks from the MACl salt are observed (shown as *). A different phase emerges when the ratio used in the preparation is decreased to 1 : 3, which was identified as $MnCl_2.2H_2O$ (shown as ⬧). These impurity phases can be distinguished as white powder attached to the crystal surface or precipitated at the bottom of the flask. Only the MAMC1 sample was free of white powder. A fit to the powder XRD pattern of sample MAMC1 using the *Cmca* space group is shown in Fig. 6.5 with the refined lattice parameters listed in table 6.3. The lattice parameters determined by powder XRD should be considered more accurate than those determined by single crystal XRD at room temperature, which are influenced by twinning; spots containing *h* and *l* components will be broadened due to the superposition of diffraction patterns from the two twin domains, which can make the a and c-parameters erroneously appear almost equal.

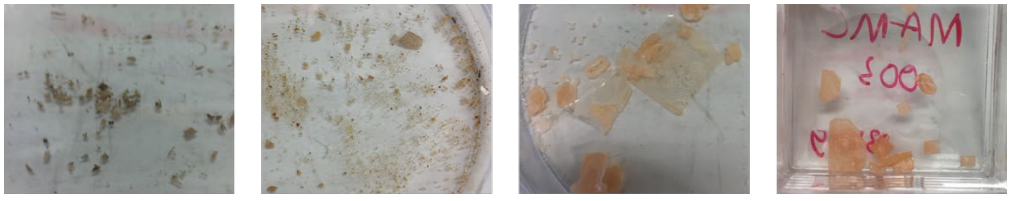

Figure 6.3 *Photos of the crystals grown in MAMC samples 1-4.*

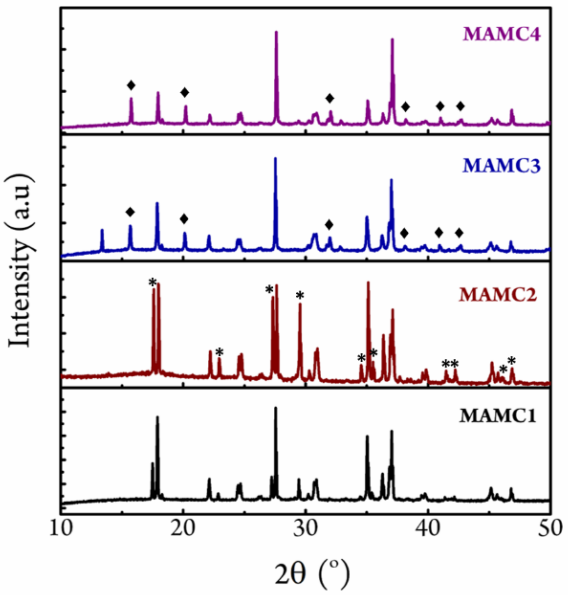

Figure 6.4 *Powder XRD patterns of MAMC samples. The asterisk (*) symbols indicate peaks of the MACl impurity phase, while the diamond (⬥) symbols indicate peaks of the $MnCl_2.2H_2O$ phase.*

Table 6.3 Unit cell parameters of sample MAMC1 determined from powder XRD measurement at 300K.

Parameters	MAMC1	Heger, et al.[2]
Space group	Cmca	Cmca
a (Å)	7.2734(6)	7.276(3)
b (Å)	19.4142(14)	19.41(1)
c (Å)	7.2126(6)	7.215(3)
V (Å^3)	1018.484	1018.95
Z	4	4
Rp	0.0548	
wRp	0.0856	
X^2	7.393	

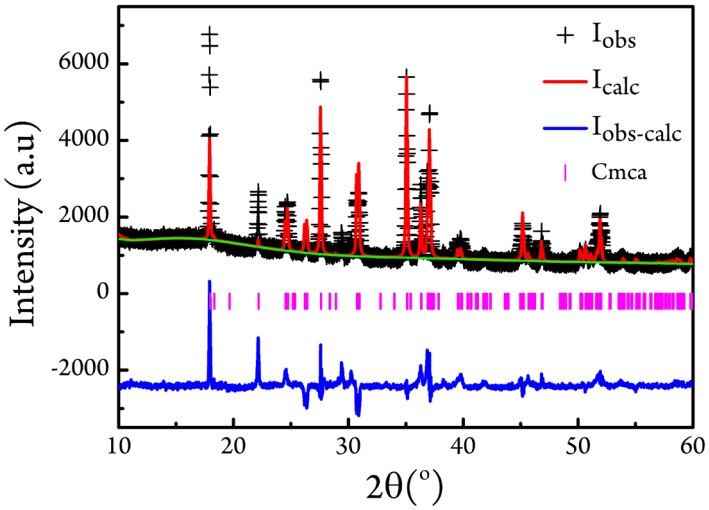

Figure 6.5 *Observed (black data points), fitted (red line) and difference (blue line) powder XRD profiles for sample MAMC1 measured at 300K.*

6.3.2 Magnetic Properties

MAMC is reported to show canted antiferromagnetism with a small net ferromagnetic moment that lies in-plane with respect to the sheets of corner shared $MnCl_6$ octahedra.[7] Temperature dependent magnetic susceptibility measurements on our crystals are in agreement with previous reports, as shown in Fig. 6.6. Magnetic anisotropy appears below T_N, where a decrease in susceptibility is observed when measured perpendicular to the $MnCl_4$ sheets, whereas a steep increase occurs when measured in-plane. This observation suggests that perpendicular to the sheets the exchange interaction is antiferromagnetic, whereas in-plane there may be a weak ferromagnetic component due to spin-canting.

Fig. 6.7 shows the temperature-dependent susceptibility of all four samples, measured in-plane. All samples show a minimum at ~45 K, which we assign as the Néel temperature (T_N) for three-dimensional ordering. Furthermore, a step-like feature is observed at ~94 K, possibly related to the previously reported structural phase transition at ~95 K from a monoclinic to tetragonal $P4_2/ncm$ structure.[2] In Fig. 6.7a, we observe a small peak for the MAMC4 sample at ~9 K, which comes from the impurity phase of $MnCl_2.2H_2O$.[29] The samples differ greatly in their response below T_N; the steepest upturn and hence largest ferromagnetic moment is found for sample MAMC1, and

for decreasing halide concentration the ferromagnetic component is strongly suppressed. This trend can clearly be seen in the derivative of the susceptibility plot in Fig. 6.8.

Field-dependent magnetization plots for sample MAMC1 are given in Fig. 6.9, measured along different crystal directions. In-plane measurement gives a plot that is close to linear, implying antiferromagnetic behaviour with a small hysteresis that opens below 1 T. The small hysteresis can be attributed to the weak in-plane ferromagnetic moment. When measured in the out-of-plane direction there is an obvious inflection point where the slope changes visibly. This is related to a spin-flop transition, where the spins rotate by 90 degrees with respect to their initial state. The field at which this spin flop transition occurs is referred to as $H_{sf,}$ and is 3.5 T for MAMC, as shown in the inset of Fig. 6.9b; this value is similar to a previous report.[1]

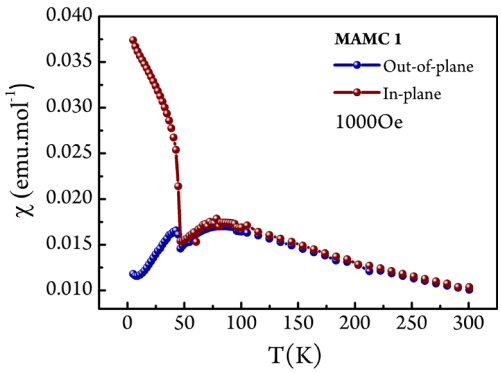

Figure 6.6 *Field-cooled temperature-dependent susceptibility of MAMC measured along different crystal directions*

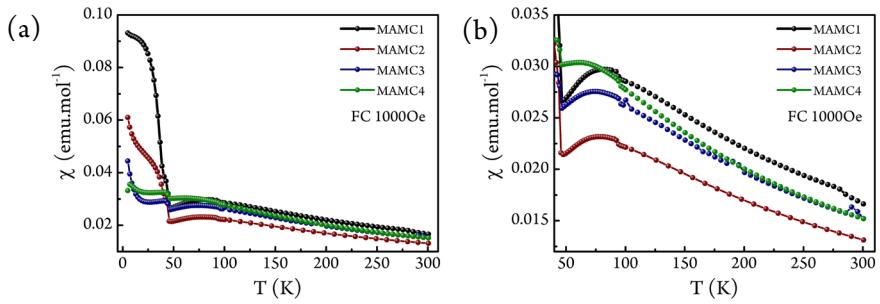

Figure 6.7 *Temperature-dependent in-plane susceptibility of all samples in the temperature range of a) 5-300 K and b) 50-300 K.*

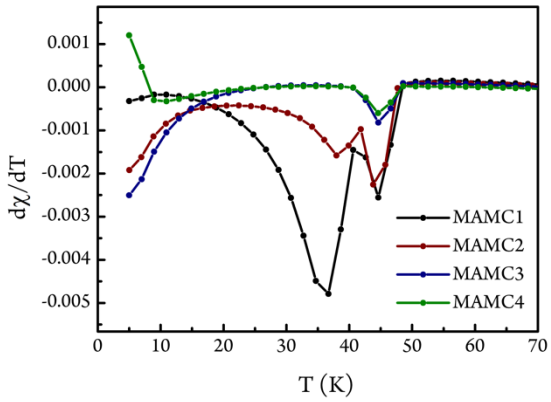

Figure 6.8 *Derivative of magnetic susceptibility versus temperature for all samples*

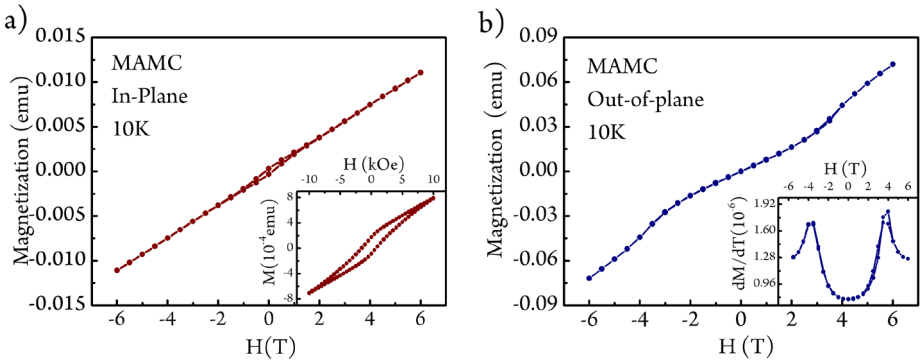

Figure 6.9 *Magnetic field dependent magnetization of sample MAMC1 measured a) in-plane and b) out-of-plane at 10 K*

MAMC is known as an ideal system in which to study 2D Heisenberg antiferromagnetism. Curély et al. formulated a model that can explain the temperature-dependent magnetic susceptibility of 2D antiferromagnets above T_N,[13–16] as detailed below. The static susceptibility depends on L, G, J, and β which are the Langevin function, Landé factor, the exchange energy, and $\beta = 1/k\mathrm{T}$, where k is the Boltzmann constant, respectively.

$$\chi = \frac{\beta G^2}{3}\left(\frac{1+L(-\beta J)}{1-L(-\beta J)}\right)^2 \tag{6.1}$$

Curély et al. also proposed an equation that estimates the temperature at which a broad maximum in the susceptibility occurs, referred to as $T(\chi_{max})$:

$$\frac{kT(\chi_{max})}{JS(S+1)} = 1.2625 \qquad (6.2)$$

Here it is assumed that S = 5/2 for high-spin Mn^{2+}.

Fig. 6.8 shows a fit to the susceptibility versus temperature plot of MAMC1 using equation (6.1), which models the curve rather well. The extracted Landé factor (G) and exchange energy (J/k_B) are 2.12 $\mu_B/\hbar$ and 7.29 K, which are comparable to the values obtained for MAMC by Curely (1.89 $\mu_B/\hbar$ and 7.23 K, respectively).[15] The Landé factor of MAMC was also determined previously as 1.9987 $\mu_B/\hbar$ by the EPR technique at 300K.[30] The extracted values for all four samples are given in Table 6.3.

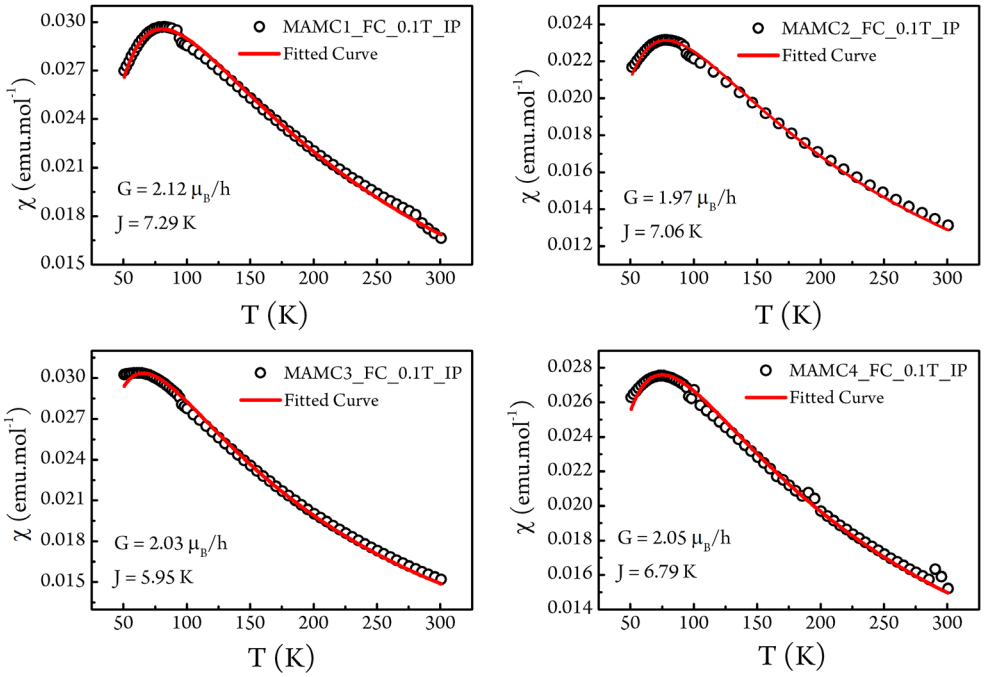

Figure 6.10 *Fit to susceptibility versus temperature curves of all four MAMC samples using 2D Heisenberg antiferromagnet model (equation 6.1)*

Table 6.3 Landé Factor, exchange energy, and theoretical / experimental temperature at χ_{max}

Compound	G	J/k_B	$T(\chi_{max})_{Th}$	$T(\chi_{max})_{Exp}$	$\Delta T(\chi_{max})_{Th}$ $/T(\chi_{max})_{Exp}$
MAMC[15]	1.89 $\mu_B/\hbar$	7.23 K	79.9 K	82.7 ± 3 K	-3.5%
MAMC1	2.12 $\mu_B/\hbar$	7.29 K	80.5 K	81.3 ± 3 K	-1%
MAMC2	1.97 $\mu_B/\hbar$	7.06 K	77.9 K	78.8 ± 2 K	-1.2%
MAMC3	2.05 $\mu_B/\hbar$	6.79 K	75.0 K	74.4 ± 2 K	+0.8%
MAMC4	2.03 $\mu_B/\hbar$	5.95 K	65.73 K	61.5 ± 3 K	+6.4%

The temperature of the broad maximum in the susceptibility also shows good agreement between the theoretical and experimental values, providing more evidence that the theoretical model is well suited to MAMC. Furthermore, we notice that as the halide concentration decreases, the exchange energy also decreases, thus lowering $T(\chi_{max})$. It is therefore useful to examine the in-plane crystal structure since the Mn-Cl-Mn distances in the corner-sharing octahedral sheets determine the primary magnetic interactions.

The relevant structural parameters of the MAMC samples are presented in table 6.4. The main differences are that for MAMC1, 2, and 3, the unit cell parameter and bond distances in the ab-plane decrease slightly with decreasing halide concentration. This may be due to local anion vacancies, which lead to an overall contraction of the structure, as also apparent from the unit cell volume. This trend is not followed for sample MAMC4 where the quantity of MA and HCl used in the synthesis was half of the stoichiometric amount with respect to $MnCl_2$. We would expect that the MAMC4 structure should be most halide-deficient and hence have the smallest unit cell volume, but as shown in Table 6.4, the opposite is the case. This might be due to the presence of solvent/water in the structure. It has been suggested that for hybrid perovskites containing MA as the organic cation, water molecules may occupy the void between inorganic layers.[31] Sample MAMC4 might also be deficient in MA cations, allowing a higher concentration of solvent/ water molecules in the inter-planar space. Nevertheless, from our observations of samples MAMC1 to MAMC3, we argue that local anion vacancies decrease the magnitude of the in-plane magnetic exchange interactions, thus shifting the position of the broad susceptibility maximum to lower temperature.

Table 6.4 Unit cell parameters, bond distances, and bond angles of MAMC samples determined at 100K

Sample	a = b (Å)	c (Å)	Mn-Cl bond length (Å)	Mn-Cl-Mn angle (°)	Mn-Mn distance(Å)	C-N bond length(Å)	Volume (Å^3)
MAMC1	7.2185(5)	19.2972(2)	2.5774(2) $_{ax}$ 2.5521(1) $_{ax}$ 2.4971(6) $_{eq}$	180 163.938(1)	5.1043(3)	1.4733(4)	1005.5(2)
MAMC2	7.2165(4)	19.2757(2)	2.5769(1) $_{ax}$ 2.5514(1) $_{ax}$ 2.4937(6) $_{eq}$	180 163.875(1)	5.1028(2)	1.4766(3)	1003.8(2)
MAMC3	7.2112(3)	19.2947(2)	2.5748(2) $_{ax}$ 2.5495(1) $_{ax}$ 2.4958(8) $_{eq}$	180 163.933(1)	5.0991(2)	1.4652(5)	1003.3(2)
MAMC4	7.2225(6)	19.3197(3)	2.5798(5) $_{ax}$ 2.5535(2) $_{ax}$ 2.5002(2) $_{eq}$	180 163.622(1)	5.1071(3)	1.4688(1)	1007.8(2)
MAMC[2]	7.23(1)	19.32(2)	2.5782(3) $_{ax}$ 2.5562(3) $_{ax}$ 2.4989(3) $_{eq}$	180 165.016(2)	5.1124(5)	1.4896(1)	1009.9(3)

The inverse magnetic susceptibility as a function of temperature is not fully linear in the range measured up to room temperature. Therefore, the effective moments of the samples could not be reliably extracted, although approximate values are rather large, in the range 6.7-7.8 μ_B/Mn. This suggests that all Mn^{2+} is in the high-spin state and there is thus no indication of SCO behavior in MAMC. It is likely that the subtle structural changes observed between the samples are too small to significantly affect the crystal field splitting energy. A previous study indicates that for a SCO to be observed, a large compression of the lattice (>20% with respect to volume) is required, which would considerably decrease the bond distances within the inorganic layer.[23] This would lead to a much larger crystal field splitting energy and hence a low-spin state.

6.4 Conclusions

A series of single crystals of the layered hybrid perovskite $(CH_3NH_3)_2MnCl_{4-x}$ have been grown with varying degrees of halide deficiency, controlled by altering the stoichiometric ratio of the precursors during synthesis. The crystal structures of the samples are in agreement with previous reports, but we find twinning in all the crystals in the orthorhombic phase at room temperature, which has not previously been reported. The variation in halide concentration does not have a significant effect on the structure of MAMC; only minor changes in the bond distances and angles are found with a consequent decrease in cell volume with increasing halide deficiency. Powder XRD measurements show the presence of the impurity phase MACl at lower halide deficiency and $MnCl_2.2H_2O$ for larger deficiency. The variation of halide concentration has a more pronounced effect on the magnetic properties. An increase in the concentration of local anion vacancies gives rise to a decrease in the magnetic exchange energy.

6.5 References

1 W. D. van Amstel and L. J. de Jongh, Solid State Commun., 1972, **11**, 1423–1429.

2 G. Heger, D. Mullen and K. Knorr, Phys. Stat. Sol. A, 1975, **31**, 455-462.

3 G. Heger, E. Henrich and B. Kanellakopulos, Solid State Commun., 1973, **12**, 1157–1165.

4 A. Ran Lim, Solid State Commun., 2017, **267**, 18–22.

5 K. Strobel, J. Frank, K. Rosshirt and R. Geick, Int. J. Infrared Millimeter Waves, 1980, **1**, 295–307.

6 N. Lehner, K. Strobel, R. Geick and G. Heger, *J. Phys. C Solid State Phys.*, 1975, **8**, 4096–4106.

7 T. Yoshinari, Phase Transitions, 1990, **28**, 79–97.

8 M. A. White, N. W. Granville and L. A. K. Staveley, J. Phys. Chem. Solids, 1982, **43**, 341–349.

9 Z. Nie, J. Yin, H. Zhou, N. Chai, B. Chen, Y. Zhang, K. Qu, G. Shen, H. Ma, Y. Li, J. Zhao and X. Zhang, ACS Appl. Mater. Interfaces, 2016, **8**, 28187–28193.

10 X. Cheng, L. Jing, Y. Yuan, S. Du, Q. Yao, J. Zhang, J. Ding and T. Zhou, CrystEngComm, 2019, **21**, 4085–4091.

11 W. Depmeier, J. Felsche and G. Wildermuth, J. Solid State Chem., 1977, **21**, 57–65.

12 H. Arend, R. Hofmann and F. Waldner, Solid State Commun., 1973, **13**, 1629–1632.

13 J. Curély, Phys. B Condens. Matter, 1998, **245**, 263–276.

14 J. Curély, Phys. B Condens. Matter, 1998, **254**, 277–297.

15 J. Curély and J. Rouch, Phys. B Condens. Matter, 1998, **254**, 298–321.

16 J. Curély and J. Kliava, Phys. Status Solidi C, 2014, **11**, 989–994.

17 K. W. Lee, C. H. Lee, C. E. Lee and J. Kang, Phys. Rev. B, 2000, **62**, 95–98.

18 E. Wortham, A. Zorko, D. Arcon and A. Lappas, Phys. B Condens. Matter, 2002, **318**, 387–391.

19 A. Abhervé, T. Grancha, J. Ferrando-Soria, M. Clemente-León, E. Coronado, J. C. Waerenborgh, F. Lloret and E. Pardo, Chem. Commun., 2016, **52**, 7360–7363.

20 H. Banerjee, S. Chakraborty and T. Saha-Dasgupta, Inorganics, 2017, **5**, 47.

21 W. W. Wu, S. G. Wu, Y. C. Chen, G. Z. Huang, B. H. Lyu, Z. P. Ni and M. L. Tong, Chem. Commun., 2020, **56**, 4551–4554.

22 A. J. Fitzpatrick, E. Trzop, H. Müller-Bunz, M. M. Dîrtu, Y. Garcia, E. Collet and G. G. Morgan, Chem. Commun., 2015, **51**, 17540–17543.

23 Y. Wang, Z. Zhou, T. Wen, Y. Zhou, N. Li, F. Han, Y. Xiao, P. Chow, J. Sun, M. Pravica, A. L. Cornelius, W. Yang and Y. Zhao, J. Am. Chem. Soc., 2016, **138**, 15751–15757.

24 H. Banerjee, A. Rittsteuer and M. Aichhorn, 2021, arXiv:2106.10675.

25 F. Aguado, F. Rodriguez and P. Núñez, Phys. Rev. B, 2007, **76**, 094417.

26 G. M. Sheldrick, Acta Crystallogr. A, 2008, **64**, 112–122.

27 B. H. Toby, J. Appl. Crystallogr., 2001, **34**, 210–213.

28 K. S. Aleksandrov and J. Bartolomé, Phase Transitions, 2001, **74**, 255–335.

29 J. N. McElearney, S. Merchant and R. L. Carlin, Inorg. Chem., 1973, **12**, 906–908.

30 K. A. Muller, A. Rigamonti and H. G. Boersch, Local Properties at Phase Transitions, North Holland Publishing Company, 1976.

31 M. I. Asghar, J. Zhang, H. Wang and P. D. Lund, Renew. Sustain. Energy Rev., 2017, **77**, 131–146.

APPENDIX

Table 6.5 Structural parameters of sample MAMC2 at different temperatures determined by single crystal XRD.

	100K	300K	400K
Crystal System	Tetragonal	Orthorhombic	Tetragonal
Space group	$P4_2/ncm$	Cmca	I4/mmm
a (Å)	7.2165(4)	7.26770(7)	5.1454(6)
b (Å)	7.2165(4)	19.4224(22)	5.1454(6)
c (Å)	19.2757(19)	7.2284(8)	19.5310(37)
V (Å^3)	1003.84	1020.33	517.09
Z	4	4	2
density (g/cm^3)	1.726	1.700	1.676
goodness of fit	1.115	1.052	1.134
R indices	0.0248	0.0884	0.0327
largest diff peak/hole	0.44/-0.71	2.08/-1.13	0.33/-0.75

Table 6.6 *Structural parameters of sample MAMC3 at different temperatures determined by single crystal XRD.*

	100K	**300K**	**400K**
Crystal System	Tetragonal	Orthorhombic	Tetragonal
Space group	$P4_2/ncm$	Cmca	I4/mmm
a (Å)	7.2112(5)	7.2544(8)	5.1498(6)
b (Å)	7.2112(5)	19.4482(27)	5.1498(6)
c (Å)	19.2947(18)	7.2523(10)	19.5501(37)
V ($Å^3$)	1003.35	1023.19	518.48
Z	4	4	2
density (g/cm^3)	1.727	1.697	1.671
goodness of fit	1.249	1.062	1.107
R indices	0.0336	0.0461	0.0354
largest diff peak/hole	0.42/-0.63	0.46/-0.66	0.31/-0.74

Table 6.7 *Structural parameters of sample MAMC4 at different temperatures determined by single crystal XRD.*

	100K	**300K**	**400K**
Crystal System	Tetragonal	Orthorhombic	Tetragonal
Space group	$P4_2/ncm$	Cmca	I4/mmm
a (Å)	7.2225(6)	7.2639(16)	5.1523(7)
b (Å)	7.2225(6)	19.4747(45)	5.1523(7)
c (Å)	19.3197(18)	7.2547(16)	19.5862(44)
V (Å^3)	1007.80	1026.27	519.94
Z	4	4	2
density (g/cm^3)	1.719	1.691	1.666
goodness of fit	1.382	1.078	0.937
R indices	0.0706	0.1178	0.0503
largest diff peak/hole	1.45/-1.16	1.28/-1.03	0.60/-0.70